Journal of Crystal Growth 625 (2024) 127438

Contents lists available at ScienceDirect

Journal of Crystal Growth

journal homepage: www.elsevier.com/locate/jcrysgro

Effects of the inert phase on solidification near a triple-phase line

Nojan Bagheri-Sadeghi, Brian T. Helenbrook *

Department of Mechanical & Aerospace Engineering, Clarkson University, Potsdam, NY 13699-5725, United States

ARTICLE INFO

Communicated by C.w. Lan

Keywords:
A1 computer simulation
A1 heat transfer
A1 interfaces
A1 solidification
A1 triple-phase line
A2 growth from melt

ABSTRACT

The local temperature solution near the triple-phase line of a solidifying front, its melt, and a surrounding inert phase was obtained analytically including all three phases and solidification kinetics. This analytical solution was validated using a three-phase numerical model of the horizontal ribbon growth of silicon and compared to a two-phase analysis that models the effect of the third phase (e.g. the gas) as an applied heat flux. Although the three-phase solutions have additional modes to represent the gas behavior, for many conditions the two-phase and three-phase models predicted consistent behaviors. However, introduction of a non-zero growth angle causes the gas phase heat fluxes to have strong gradients near the triple-phase line. Even with zero growth angle, there are conditions in which the two-phase and three-phase solutions are very different; one predicting infinite heat fluxes while the other predicts finite fluxes. This depended on the ratios of thermal conductivities, and the angle at which the solid-melt interface intersected the free surface. In particular, when the thermal conductivity of the inert phase was comparable to the melt or solid phases there were significant differences.

1. Introduction

Triple-phase line (also called a tri-junction, a three-phase contact line, or a triple junction) of a crystal, melt and inert phase, appears in many systems where crystals grow from their melt. The inert phase can either be a crucible wall, such as in Bridgman–Stockbarger growth, or a gas, such as in droplet solidification and the Czochralski, float zone, or horizontal ribbon growth (HRG) methods. For all of these configurations, the conditions at the triple-phase line can have a significant effect on the shape, position, and evolution of the solidification front [1].

Fig. 1 shows a schematic of a two-dimensional triple-phase line (with the triple-phase line being a point in 2D) formed in a solidification system where a non-participating inert phase is present. The position of the triple-phase line is designated as center of the coordinate system O_{TPL} with angles defined positive counterclockwise from the x^* axis. The solid angle, θ_s, is the angle between the growth front and the solid surface which is assumed horizontal. The solid angle is often determined by the crystallography of the growth. For example, in HRG the pull direction is typically the [011] direction and the growth is aligned with a (111) facet which results in a $\theta_s = 55°$ or a $(\bar{1}11)$ facet with $\theta_s = 125°$ depending on which {111} plane the growth aligns with (see Refs. [2,3]). The growth angle, θ_{gr}, is the angle formed between the melt-gas interface and the velocity vector of the triple-phase line in a frame of reference moving with the solid. It is equivalent to the angle formed between tangents to the melt-gas and the solid-gas interfaces as shown in Fig. 1 [4]. However, it is really a condition on the direction of growth of the triple-phase line. In non-solidifying cases, the growth angle is not relevant and the triple-phase line is simply a pinning point for the liquid-gas interface. Such a condition on the direction of growth of a triple-phase line is important for unsteady simulations involving a moving triple-phase line where there could be waves on the solid and liquid surfaces (e.g. see [5]). For confined solidification systems like Bridgman–Stockbarger or gradient freeze methods the inert phase is a solid wall and thus $\theta_{gr} = 0$ [6]. In Fig. 1, the solid crystal is being pulled at a horizontal speed of $u_{s,1}$. When a steady process is established, with the growth rate and pull speeds balanced, the triple-phase line becomes stationary. An inertial frame of reference in which the triple-phase line is stationery is used throughout the paper. In some of the following, indicial notation is used where the subscripts 1 or 2 when referring to velocity (such as $u_{s,1}$) or position correspond to horizontal or vertical directions respectively.

Anderson and Davis [7] analytically studied two-phase non-isothermal flow and determined the temperature and flow fields of the liquid and inert phases near a two-dimensional triple-phase line like the one shown in Fig. 1. Considering the combinations of adiabatic and fixed temperature boundary conditions along the solid–liquid and solid-inert phase interfaces, they determined the local behavior of the heat fluxes and stresses near the triple-phase line and identified conditions of their singular or regular behavior extending previous singular point analysis of single and two-phase isothermal flows near a wedge [8–11]. Singularities, e.g. unbounded derivatives of temperature, could

* Corresponding author.
E-mail address: bhelenbr@clarkson.edu (B.T. Helenbrook).

https://doi.org/10.1016/j.jcrysgro.2023.127438
Received 10 August 2023; Received in revised form 30 September 2023; Accepted 2 October 2023
Available online 5 October 2023

Nomenclature

English Symbols

A	constant term of the horizontal temperature gradient of the analytical solution, K/m
A_{2DN}	constant of two-dimensional nucleation kinetics, K
B	constant term of the vertical temperature gradient of the analytical solution, K/m
B_{2DN}	constant of two-dimensional nucleation kinetics, K s/m
c	specific heat, J/(kg K)
d	depth of the melt at the inlet, m
d_{TPL}	depth of triple-phase line from the horizontal melt-gas interface, m
F	view factor function
F_b	function used to model the locality of the heater at the bottom of the melt
g	gravitational acceleration, m/s^2
h	height of the jet exit from the horizontal melt-gas interface, m
h_c	height of the lower edge of the vertical wall of the jet injector from the horizontal melt-gas interface, m
k	thermal conductivity, W/(m K)
K_{2DN}	two-dimensional nucleation kinetics coefficient, K s/m
K_{rough}	roughened growth kinetics coefficient, K s/m
K_{SN}	constant of step propagation kinetics coefficient, K s/m
K_{step}	step propagation kinetics coefficient, K s/m
L_f	latent Heat of Fusion, J/kg
Ma	Mach number
n	outward unit normal vector
p	pressure, Pa
p_{atm}	atmospheric pressure, Pa
q	heat flux, W/m^2
q_b	heat flux distribution from the heater at the bottom of the melt, W/m^2
q_H	peak heat flux from the heater at the bottom of the melt, W/m^2
r	radial coordinate, m
R_{He}	helium gas constant, J/(kg K)
Re	Reynolds number
T	temperature, K
T_c	temperature of cold helium exiting from the jet slot, K
T_m	equilibrium melting temperature, K
T_w	temperature of the vertical walls of the jet injector, K
u	velocity, m/s
V_g	growth rate, m/s
V_s	average jet velocity, m/s
w	total width of the jet injector, m
w_1	width of horizontal walls on sides of the jet exit, m
w_2	width of angled walls of the jet, m
w_b	half-width of the heater used at the bottom of the melt, m
w_s	slot jet width, m
x	spatial coordinate, m

Greek Symbols

α	angle of jet walls, rad
ΔT	degree of supercooling, K
ϵ	emissivity
κ	mean interface curvature, 1/m
λ	eigenvalue of homogeneous solution
μ	dynamic viscosity, kg/(m s)
Ω	physical subdomain
ϕ_i	parameters of the view factor $i \in 1,2$
ρ	density, kg/m^3
σ	surface tension, N/m
σ_B	Stefan–Boltzmann constant, W/(m^2 K^4)
τ	stress tensor, Pa
θ	angular coordinate, rad
θ_s	solid angle, rad
θ_{gr}	growth angle, rad
θ_{lg}	angle of the melt-gas interface, rad
θ_m	misalignement angle, rad

Subscripts

$2ph$	two-phase model
$3ph$	three-phase model
g	gas
h	homogeneous solution
i	index identifying the subdomain (i.e. solid, liquid or gas)
l	melt
p	particular solution
rad	radiation
s	solid
TPL	triple-phase line

imply that the configuration is non-physical, there are deficiencies in the continuum model, or there is a breakdown of the continuum approximations.

In a subsequent paper [12], they performed a singular point analysis of a triple-phase line where solidification occurred. They specified a jump in the heat flux equal to the latent heat of fusion along the solid-melt interface and assumed the solidification interface to be at the equilibrium melting temperature T_m with adiabatic conditions at the solid-gas and melt-gas interfaces. They showed that with these boundary conditions, the free surfaces of solid and melt must form right angles with the solid-melt interface.

Helenbrook [13] extended the work of [12] by studying the effect of non-zero heat flux at the solid-gas and melt-gas interfaces, again assuming the interface to be at T_m. He showed that when these heat fluxes are continuous at the triple-phase line the solidification front intersects the upper surface at 0°, i.e. in a cusp, which is significantly different than when the gas interfaces are adiabatic. However, he showed that with a discontinuous heat flux (e.g. due to discontinuity in the emissivity of solid and melt) or in the presence of a growth angle, various solid angles are possible.

Pirnia and Helenbrook [3,14] included the effects of supercooling along the solidifying interface by incorporating solidification kinetics. They performed a two-phase analysis (modeling the inert gas phase as

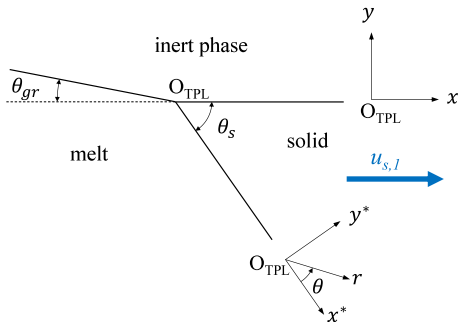

Fig. 1. Schematic of a triple-phase line for meniscus-defined solidification from a melt where the inert phase is a fluid (i.e. gas or liquid). For a confined solidification system the inert phase is a solid wall and $\theta_{gr} = 0$.

an applied heat flux) of the local behavior of the temperature field near the triple-phase line and determined the conditions that led to singular temperature gradients at the triple-phase line.

In all of the above analyses, the inert phase effect (i.e. the solid wall or inert fluid) is modeled by a constant heat flux (sometimes with a jump at the triple-phase line) [3,13,14], however, the validity of this assumption is not clear especially considering the large temperature gradients that are in the melt and solid. The purpose of this paper is to extend the two-phase analysis of the temperature field near the triple-phase line by Helenbrook and Pirnia [3] by including all three phases and to determine the importance of including the inert phase by comparing the heat flux behavior predicted by the two-phase [3] and three-phase analyses. The analysis applies to both meniscus-defined solidification and confined solidification systems where $\theta_{gr} = 0$ and the solidification occurs along a solid wall. Any significant discrepancies between these two demonstrate the importance of including the inert phase in numerical or analytical models. The results are validated by three-phase numerical simulations of HRG, which are the first three-phase simulations of this process ever performed.

2. Methods

2.1. Analytical model near the triple-phase line

The three interfaces near the triple-phase line are shown in Fig. 1 where in terms of solid angle, θ_s, and the growth angle, θ_{gr}, the solid, inert, and melt phases respectively correspond to $0 \le \theta \le \theta_s$, $\theta_s \le \theta \le \theta_{lg}$, and $\theta_{lg} \le \theta \le 2\pi$ where $\theta_{lg} = \theta_s + \pi - \theta_{gr}$. Note that the subscripts s, l, and g indicate the solid, liquid, and inert phases. The subscript g is used for the inert phase because, in the HRG application, it is a gas but the inert phase could also be a solid, with $\theta_{gr} = 0$, for confined solidification systems. The two coordinates shown are centered at the triple-phase line and are aligned with the interfaces.

Faceted growth was assumed to occur on the melt-solid interface where the misalignment angle between the solidification front and the facet direction, θ_m, is governed by step-nucleation kinetics through the relation [15]

$$\Delta T = K_{step} V_g = \frac{K_{SN}}{|\sin(\theta_m)|} V_g, \tag{1}$$

where $\Delta T = T - T_m$ is the degree of supercooling on the interface with T and T_m denoting temperature and the equilibrium melting temperature respectively; K_{step} is the step propagation kinetics coefficient; K_{SN} is the constant of step nucleation; and V_g is the growth rate. The misalignment angle was assumed to be small such that to leading order the solid angle is aligned with the facet. As shown below, this allows us to determine the temperature along the facet without knowing the misalignment angle. At the triple-phase line, it was assumed that two-dimensional nucleation occurs. This determines the temperature at the triple-phase line through

$$\Delta T = K_{2DN} V_g = B_{2DN}^{-1} e^{\frac{A_{2DN}}{\Delta T}} \Delta T V_g, \tag{2}$$

where K_{2DN} is the coefficient of two-dimensional nucleations and A_{2DN} and B_{2DN} are constants. Table 1 gives kinetic coefficients although really only the 2D nucleation coefficients were used in the analytic results. The other coefficients were used for the full numerical simulations described subsequently.

Table 1
The solidification kinetics parameters.

Parameter	Value	Unit
A_{2DN}	140 [15]	K
B_{2DN}	1.5×10^{10} [15]	m/(s K)
K_{SN}	1/0.63 [16]	K s/m
K_{rough}	1/0.122 [17]	K s/m

To determine the temperature in the vicinity of the triple-phase line, steady-state conservation of energy was used. This reduces to Laplace's equation for the temperature, T, as the convective terms in the energy equation are small compared to the diffusion terms (see [3,13]),

$$\frac{1}{r}\frac{\partial}{\partial r}\left(r\frac{\partial T_i}{\partial r}\right) + \frac{1}{r^2}\frac{\partial^2 T_i}{\partial \theta^2} = 0, \tag{3}$$

where the subscript $i \in \{g, l, s\}$ identifies the phase. The simplification of the energy equation to the form shown above is valid where the Peclet number Pe_i based on r, $\rho_i c_i u_{s,1} r/k_i$ is much less than one [13,14], where ρ is density, c is specific heat at constant pressure, and k is the thermal conductivity.

Temperature continuity at the interfaces leads to the following three boundary conditions:

$$T_l(r, 2\pi) = T_s(r, 0), \tag{4a}$$

$$T_s(r, \theta_s) = T_g(r, \theta_s), \tag{4b}$$

$$T_g(r, \theta_{lg}) = T_l(r, \theta_{lg}). \tag{4c}$$

Three additional boundary conditions result from conservation of energy at the interfaces:

$$-\frac{k_l}{r}\frac{\partial T_l}{\partial \theta}\bigg|_{\theta=2\pi} + \frac{k_s}{r}\frac{\partial T_s}{\partial \theta}\bigg|_{\theta=0} = -\rho_s L_f u_{s,1} \sin\theta_s, \tag{5a}$$

$$-\frac{k_s}{r}\frac{\partial T_s}{\partial \theta}\bigg|_{\theta=\theta_s} + \frac{k_g}{r}\frac{\partial T_g}{\partial \theta}\bigg|_{\theta=\theta_s} = q_{rad,s}, \tag{5b}$$

$$-\frac{k_g}{r}\frac{\partial T_g}{\partial \theta}\bigg|_{\theta=\theta_{lg}} + \frac{k_l}{r}\frac{\partial T_l}{\partial \theta}\bigg|_{\theta=\theta_{lg}} = q_{rad,l}. \tag{5c}$$

where L_f is the latent heat of fusion, and $q_{rad,i}$ with $i \in \{l, s\}$ is the net radiation heat flux from the melt and solid surfaces. It was assumed that the liquid and solid are completely opaque so that all radiation is emitted and absorbed at the interface. These radiation heat fluxes would be 0 for growth problems with a solid inert phase. As this expansion is for $r \ll 1$ the spatial variation of the radiation fluxes was neglected.

To completely define the temperature solution near the triple-phase line, an additional boundary condition along a circle of finite radius surrounding the triple-phase line is needed, which is unknown. However, the known boundary conditions (4)a–(4)c and (5)a–(5)c can still be used to determine the behavior of the solution as $r \to 0$. For this set of linear differential equations and boundary conditions, the solution can be written as the sum of the solution of Laplace's equation with homogeneous boundary conditions and a particular solution satisfying the nonhomogeneous boundary conditions.

2.1.1. The homogeneous solution

The homogeneous solution satisfies the temperature continuity conditions (4)a–(4)c and energy conservation Eqs. (5)a–(5)c with zero right-hand sides. Assuming a separable homogeneous solution as $T_{i,h}(r,\theta) = \eta_i(r)\psi_i(\theta)$, and substituting into Eq. (3) gives

$$\frac{r}{\eta_i}\frac{\partial}{\partial r}\left(r\frac{\partial \eta_i}{\partial r}\right) = -\frac{1}{\psi_i}\frac{\partial \psi_i^2}{\partial \theta^2} = \lambda_i^2.$$

A nontrivial solution is obtained as $\psi_i(\theta) = C_i\cos(\lambda_i\theta) + D_i\sin(\lambda_i\theta)$ and $\eta(r) = E_i r^{\lambda_i} + F_i r^{-\lambda_i}$. Assuming λ_i values to be positive, F_i must be 0 to have a finite temperature at $r = 0$. Furthermore, the temperature continuity boundary conditions can only hold if $\lambda_s = \lambda_l = \lambda_g = \lambda$. Thus, the assumed homogeneous solution becomes of the form $T_{i,h} = \left(G_i\cos(\lambda\theta) + H_i\sin(\lambda\theta)\right) r^{\lambda}$, and the temperature continuity conditions become

$$G_l\cos(2\pi\lambda) + H_l\sin(2\pi\lambda) = G_s, \tag{6a}$$

$$G_s\cos(\lambda\theta_s) + H_s\sin(\lambda\theta_s) = G_g\cos(\lambda\theta_s) + H_g\sin(\lambda\theta_s), \tag{6b}$$

$$G_l\cos(\lambda\theta_{lg}) + H_l\sin(\lambda\theta_{lg}) = G_g\cos(\lambda\theta_{lg}) + H_g\sin(\lambda\theta_{lg}). \tag{6c}$$

and the energy conservation boundary conditions become

$$k_s H_s - k_l\left(-G_l\sin(2\pi\lambda) + H_l\cos(2\pi\lambda)\right) = 0, \tag{7a}$$

$$k_g\left(-G_g\sin(\lambda\theta_s) + H_g\cos(\lambda\theta_s)\right) - k_s\left(-G_s\sin(\lambda\theta_s) + H_s\cos(\lambda\theta_s)\right) = 0, \tag{7b}$$

$$k_l\left(-G_l\sin(\lambda\theta_{lg}) + H_l\cos(\lambda\theta_{lg})\right) - k_g\left(-G_g\sin(\lambda\theta_{lg}) + H_g\cos(\lambda\theta_{lg})\right) = 0. \tag{7c}$$

These equations can be written in matrix form for the six solution constants. To have a nontrivial solution the determinant of the matrix of coefficients of this system of linear equations should be zero. After substituting for angles in terms of θ_{gr} and θ_s the determinant simplifies to

$$\begin{aligned}
&(k_l - k_s)\Big(\,(k_g + k_s)(k_g - k_l)\cos\big(2\lambda(\theta_s - \theta_{gr})\big)\\
&-(k_g - k_s)(k_g + k_l)\cos\big(2\lambda(\pi - \theta_s)\big)\,\Big)\\
&-(k_l + k_s)\Big(\,(k_g - k_s)(k_g - k_l)\cos(2\lambda\theta_{gr})\\
&-(k_g + k_s)(k_g + k_l)\cos(2\lambda\pi)\,\Big) - 8k_g k_l k_s = 0,
\end{aligned} \tag{8}$$

which was solved numerically for eigenvalues λ_n, $n = 1..\infty$. For each value of λ_n, the null space of the coefficient matrix corresponds to an eigenvector that determines the six solution values up to a scaling constant C_n. This eigenvector is normalized to have unit length and the homogeneous solution can then be written as

$$T_{i,h}(r,\theta) = \sum_{n=1}^{\infty} C_n\left(G_{i,n}\cos(\lambda_n\theta) + H_{i,n}\sin(\lambda_n\theta)\right) r^{\lambda_n}. \tag{9}$$

The values of λ_n in this expression reveal the nature of the solution as $r \to 0$. At the triple-phase line if $\lambda_1 < 1$, the temperature gradients become singular. This can imply a breakdown in the continuum model or that important physics were neglected in the model. It may also be possible to determine which configurations are more physically likely based on the singular or non-singular behavior near $r = 0$.

Pirnia and Helenbrook [3], performed a two-phase analysis of the temperature field near the triple-phase line modeling the inert phase by constant heat fluxes and neglecting the presence of a growth angle. We have extended that result to non-zero growth angles. The homogeneous solution has the same form as Eq. (9) with the eigenvalues determined from

$$(k_s - k_l)\sin\left(\lambda(2\theta_s - \pi - \theta_{gr})\right) + (k_s + k_l)\sin\left(\lambda(\pi + \theta_{gr})\right) = 0. \tag{10}$$

One of the goals of this work is to determine when the two-phase predictions are consistent with the three-phase results.

2.1.2. The particular solution

Assuming a linear particular solution $T_{i,p} = T_{TPL} + A_i x + B_i y$, with $i \in \{g, l, s\}$, the temperature continuity conditions (Eqs. (4)a–(4)c) and the energy conservation equations (Eqs. (5)a–(5)c) reduce to a system of six linear equations in six unknowns. This linear system of equations can be solved for the A_i and B_i values. MATLAB®'s symbolic toolbox was used to obtain a symbolic solution. The particular solution was lengthy but for the special case of $\theta_{gr} = 0$ it reduces to a simple form with

$$A_l = A_s = A_g = \frac{\rho_s L_f u_{s,1}}{k_l - k_s} - \frac{q_{s,rad} - q_{l,rad}}{k_l - k_s}\cot(\theta_s), \tag{11a}$$

$$B_l = B_s = \frac{q_{s,rad} - q_{l,rad}}{k_l - k_s}, \tag{11b}$$

$$B_g = \frac{k_l q_{s,rad} - k_s q_{l,rad}}{k_g(k_l - k_s)}. \tag{11c}$$

When $q_{l,rad} = q_{s,rad} = q_{rad}$ this becomes even simpler with $A_s = A_l = A_g = \frac{\rho_s L_f u_{s,1}}{k_l - k_s}$, $B_l = B_s = 0$ and $B_g = \frac{q_{rad}}{k_g}$, which is just a linear function of x through both the solid and melt; The difference in thermal conductivities is crucial to balance the latent heat term due to solidification. Also, it is interesting that the heat flux associated with the particular solution is entirely horizontal in melt and solid. This implies that in a problem like HRG where the heat removal is primarily vertical, the homogeneous solution must play an important role.

The two-phase particular solution defined by Pirnia and Helenbrook [14] for zero growth angle is

$$T_{i,p,2ph} = T_{TPL} + \left(\frac{\rho L_f u_{s,1}}{k_l - k_s} - \frac{q_s - q_l}{k_l - k_s}(\cot\theta_s + \tan\theta_s) - \frac{q_i}{k_i}\right)x - \frac{q_i}{k_i}y, \tag{12}$$

where q_i, $i \in l, s$ denotes the sum of convective and radiative heat fluxes at the surfaces. It can be extended to non-zero growth angles following the same procedure as used above for the three-phase case. Note that the particular solutions of two-phase and three-phase analysis are different. For example, when there is no growth angle and no jump in heat flux at the triple-phase line, there is an additional horizontal temperature gradient in the two-phase particular solution equal to $-\frac{q_i}{k_i}$ and more significantly a vertical temperature gradient equal to $-\frac{q_i}{k_i}$, which does not exist in the three-phase particular solution.

2.2. Numerical model

To validate the analytical results, a simulation of HRG of silicon was used. This is similar to what was done in [5,18], however, in this work, the gas phase was also included in contrast to [5,18] where a heat flux was imposed as a boundary condition on the melt and solid surfaces. Buoyancy and Marangoni effects, included in [5], were neglected here to make the comparison of the two-phase and three-phase results simpler. Neglecting these avoids the resulting unsteady chaotic flow, allowing steady-state solutions to be obtained.

Fig. 2 shows a schematic of the simulation domain and a sample grid. The solid, melt, and gas phases are designated as Ω_s, Ω_l, and Ω_g where the gas phase was assumed to be helium. The jet slot was centered at $x_1 = 0$ with a width of $w_s = 0.15$ mm. A slot inlet section of length $2w_s$ was simulated to allow the jet to evolve naturally at the slot exit. The helium jet exited from the slot at $x_2 = h = 2$ mm. Note that due to the growth angle, the solid surface is at $x_2 = -d_{TPL}$ where d_{TPL} is the depth of the triple-phase line. The other dimensions shown in Fig. 1 are $w_1 = 0.5$ mm, $w_2 = 1.5$ mm, $\alpha = 45°$, $w = 33.5$ mm, and $h_c = 4.6$ mm. The corners of the geometry at $x_1 = \pm w_s/2$, $\pm(w_s/2 + w_1)$, $\pm(w_s/2 + w_1 + w_2)$ and $\pm w/2$, were filleted with radii of 0.05, 0.2, 0.5, and 1 mm respectively.

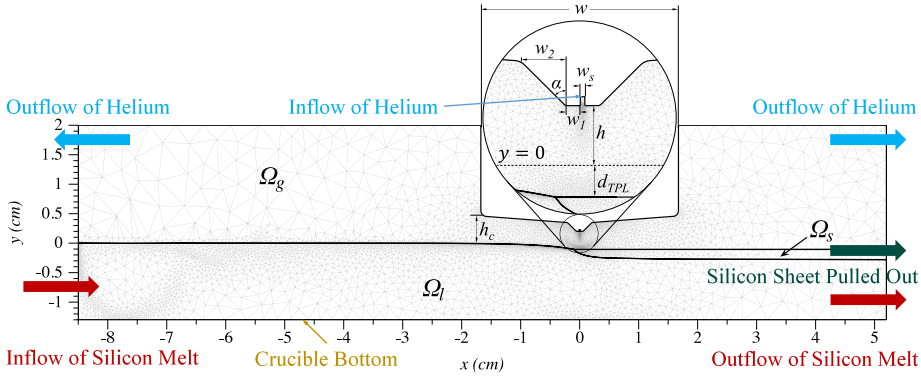

Fig. 2. Schematic and a sample mesh. The numerical resolution is 4 times finer than the mesh shown as fourth-degree basis functions were used.

Table 2
The thermophysical properties used in simulations. R_{He} is the helium gas constant.

Parameter	$i = s$	$i = l$	$i = g$	Units
ρ_i	2530 [20]	2530 [20]	$\frac{P_{atm}}{R_{He}T}$	kg/m^3
c_i	1000 [20]	1000 [20]	$\frac{5R_{He}}{2} = 5196$ [21]	J/(kg K)
k_i	22 [20]	64 [20]	0.352 [19]	W/(m K)
μ_i	–	7×10^{-4} [20]	4.46×10^{-5} [22]	kg/(m s)

Table 3
The interface parameters used in simulations.

Parameter	Value	Unit
σ	0.735 [20]	N/m
L_f	1.8×10^6 [20]	J/kg
ϵ_s	0.6 [20]	–
ϵ_l	0.2 [20]	–

2.2.1. Governing equations

The temperature field was determined by solving steady conservation of energy assuming a constant thermal conductivity in each phase $i \in \{g, l, s\}$,

$$\nabla \cdot (\rho_i c_i T_i \vec{u}_i) - k_i \nabla^2 T_i = 0, \tag{13}$$

where $\vec{u}_i = [u_{i,1}\ u_{i,2}]^T$ is the liquid, solid or gas velocity. It was assumed that the solid has a rigid body translation with a constant horizontal pull speed of $u_{s,1} = 0.7$ mm/s and $u_{s,2} = 0$. The properties used are given in Table 2. For helium, the ideal gas law was used with a constant atmospheric pressure to determine the density. The thermal conductivity of helium was evaluated at a film temperature of $\frac{T_m+T_c}{2}$ from [19] where $T_m = 1685$ K and $T_c = 300$ K is the temperature of the cold helium exiting from the jet slot.

For the gas and melt phases, the Navier–Stokes equations for a Newtonian fluid were solved to determine the flow velocities. The melt density was assumed constant so there are no buoyancy effects in the melt. The steady conservation of mass and linear momentum in phase $i \in \{g, l\}$ can be written as

$$\nabla \cdot \left(\rho_i \vec{u}_i\right) = 0, \tag{14}$$

$$\nabla \cdot \left(\rho_i \vec{u}_i \vec{u}_i\right) = -\nabla p_i + \nabla \cdot \boldsymbol{\tau_i} + \rho_i \vec{g}, \tag{15}$$

where both fluids were assumed to be Newtonian with the stress tensor given as $\boldsymbol{\tau_i} = \mu_i \left(\nabla \vec{u}_i + (\nabla \vec{u}_i)^T\right)$, $\vec{g}$ is the gravitational acceleration, and the viscosities are given in Table 2. The gas viscosity was again evaluated at the film temperature using a power law correlation [22].

2.2.2. Interface and boundary conditions

At the solid-melt interface, a Dirichlet boundary condition for melt velocity was imposed as $u_{l,1} = u_{s,1}$ and $u_{l,2} = 0$, which satisfies the conservation of mass at the interface assuming $\rho_s = \rho_l$. Also, conservation of energy at the solid-melt interface was imposed as

$$-k_s \nabla T_s \cdot \hat{n}_s - k_l \nabla T_l \cdot \hat{n}_l = \rho_s L_f \vec{u}_s \cdot \hat{n}_s, \tag{16}$$

where $\hat{n}_i$ denotes the outward unit normal vectors of surfaces [23] and L_f is given in Table 3.

Additionally, the degree of supercooling at the interface was determined based on the solidification kinetics model of [15],

$$\Delta T = K(\Delta T, \theta_m) V_g, \tag{17}$$

where θ_m is the misalignment angle from the (111) facet direction. Assuming the crystal is oriented with $[\bar{1}00]$ pointing upward and [011] to be aligned with the horizontal direction, perfectly faceted growth would correspond to a solid angle of 55°. The growth at the triple-phase line was assumed to be dislocation-free and thus the degree of supercooling was determined from two-dimensional nucleation kinetics given in Eq. (2) [15]. The growth along the rest of the solid-melt interface was assumed to be governed by step propagation and roughened growth kinetics as $K = \left(K_{step}^4 + K_{rough}^4\right)^{1/4}$ where K_{step} is given in Eq. (1) and K_{rough} is the coefficient of roughened growth given in Table 1. As the misalignment angle increases the solidification kinetics gradually transitions from step propagation to roughened growth. Note that the step kinetics constant K_{SN} was multiplied by 10 to find K_{step} as convergence was difficult when using the physically-correct value of K_{SN}. This does not cause a significant change in simulation results as shown in [24].

At the gas-solid and gas-melt interfaces, a net radiation heat flux from the melt and solid was specified as $q_{rad,i} = \epsilon_i \sigma_B F(x_1)(T_i^4 - T_c^4)$ where ϵ_i is emissivity given in Table 3, $\sigma_B = 5.678 \times 10^{-8}$ W/(m^2 K^4) is the Stefan–Boltzmann constant, and the view factor was $F(x_1) = \left(\sin\phi_2 - \sin\phi_1\right)/2$, $\sin\phi_1 = \left(-w_1 - x_1\right)/\sqrt{\left(-w_1 - x_1\right)^2 + h^2}$, and $\sin\phi_2 = \left(w_1 - x_1\right)/\sqrt{\left(w_1 - x_1\right)^2 + h^2}$ [25]. This models the radiation between the silicon and the cold walls surrounding the jet assuming that the walls are black and the silicon surface is gray, opaque, and diffuse.

At the solid-gas interface, a Dirichlet boundary condition for gas was specified as $\vec{u}_g = \vec{u}_s$. At the melt-gas interface, a zero normal velocity was imposed as the gas and melt were assumed to be immiscible. Also, along this interface a jump in normal stresses from gas to melt was imposed due to surface tension, σ, given in Table 3, as $-2\sigma\kappa$ where $\kappa = -\frac{1}{2}\nabla \cdot \hat{n}_l$ is the mean interface curvature [26]. The surface tension was assumed to be independent of temperature to avoid Marangoni flow instabilities.

In the melt subdomain, an inflow boundary condition was defined at the left side as a fully developed laminar channel flow with a velocity

profile of $u_{l,1} = -6\frac{x_2}{d}\left(1+\frac{x_2}{d}\right)u_{s,1}$, $u_{l,2} = 0$ where $d = 1.3$ cm is the depth of the melt at the inlet. The inflow was assumed isothermal with a temperature of $T = T_m + 5 = 1690$ K. The bottom of the melt was defined as a no-slip wall with a specified heat flux q_b. The heat flux modeled a heater of width $2w_b = 20.5$ mm used in HRG experiments as $q_b = q_H F_b(x_1)$ where $q_H = 16.63$ W/cm^2 and $F_b(x_1) = \frac{w_b - x_1}{2\sqrt{(w_b-x_1)^2+(0.1d)^2}} - \frac{-w_b - x_1}{2\sqrt{(-w_b-x_1)^2+(0.1d)^2}}$. $F_b(x_1)$ transitions from 0 to 1 near $x_1 = -w_b$ and then from 1 to 0 near $x_1 = w_b$ to model the locality of the heater. At the right side of the melt, an outflow boundary condition was used, specifying zero total stresses and zero diffusive heat flux. Likewise, in the solid subdomain, the right side was a zero diffusive heat flux boundary condition.

The left and right sides of the gas subdomain were also outflow boundary conditions. The inflow of helium gas to the slot jet was assumed to be a fully developed laminar channel flow at T_c, with $u_{g,2} = -\frac{3}{2}V_s\left(1-(\frac{2x_1}{w_s})^2\right)$ where the average jet velocity $V_s = 48.15$ m/s. Based on the width of the impinging slot jet, $2w_s$, the speed of sound, and the viscosity of helium at T_c, the jet Reynolds and Mach numbers were $Re = 119$ and $Ma = 0.047$. Thus, the flow can be considered incompressible and laminar as transition to turbulence for impinging jets occurs at $1000 < Re < 3000$ [27] and the Mach number is less than 0.1.

All walls associated with the helium jet including the top surfaces of the domain were no-slip. The interior, bottom, and 45°-sloped walls of the slot jet were assumed to be at T_c. The vertical exterior walls of the jet injector were assumed to be at $T_w = 1500$ K. Along the sloped bottom surface, the temperature smoothly transitioned from T_w to T_c using a fifth-order polynomial such that $\frac{\partial T}{\partial x_1}$ and $\frac{\partial^2 T}{\partial x_1^2}$ were zero at both ends. This prevented unnecessary mesh refinement by the mesh adaptation scheme. Similarly, for the top walls extending to the left and right side of the domain, a smooth transition between T_w and $T_m + 2 = 1687$ K was used, which is slightly colder than the inflowing melt temperature of 1690 K.

2.2.3. Solution method

To obtain numerical solutions, a continuous high-order finite element method (*hp*-FEM) with fourth-degree basis functions on triangular elements was used for spatial discretization with a streamline upwind Petrov–Galerkin (SUPG) stabilization approach for equal-order pressure and velocity approximation spaces [23,26,28]. To track the interfaces and maintain mesh quality an arbitrary Eulerian–Lagrangian (ALE) moving mesh method was utilized. Furthermore, a local mesh adaptation scheme was employed to obtain a uniform truncation error and improve the solution accuracy [23]. A restriction on the minimum element size was imposed to avoid excessive mesh refinement near singular points.

The solution strategy involved starting with a fixed initial interface shape at T_m as given in Ref. [5] to obtain an initial steady temperature and flow field (i.e. Eqs. (16) and (17) were neglected). As the convergence with the full gas flow rate was difficult, this initial solution was obtained with a specified convective heat flux along the gas-melt and solid-melt interfaces and only a small fraction of the actual gas flow rate. Then, an adaptive time stepping was used to obtain a steady solution while the melt-solid interface moved using ALE moving mesh and mesh adaptation. During time stepping, the gas flow rate was gradually increased to its actual value while the specified heat flux was reduced to zero. The unsteady equations used during time-stepping are given in [23,26]. Once an initial steady solution was obtained, it was possible to slightly increase the pull speed and solve the steady equations given in Sections 2.2.1 and 2.2.2 to obtain the solution at higher pull speeds. At each step, the Newton–Raphson method was applied to solve the system of equations for the shape of all interfaces, temperature, and flow velocity components, where the system Jacobian matrix was inverted using the MUMPS solver in PETSc [29].

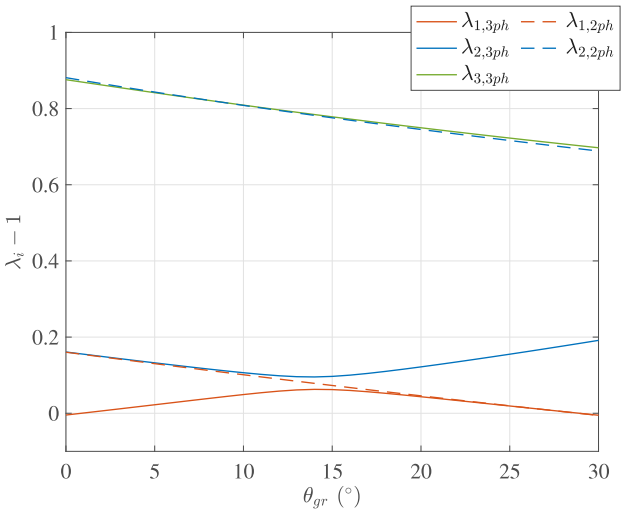

Fig. 3. The variation of the leading order eigenvalues of the analytical homogeneous solution with the growth angle θ_{gr} near the triple-phase line of a solid in contact with its melt with $\theta_s = 55°$, $k_s/k_l = 0.34$, and $k_g/k_l = 0.0055$.

3. Results and discussion

As shown in Section 2.1, near the triple-phase line the temperature in each phase changes as $T_i(r,\theta) = T_{i,h}(r,\theta) + T_{i,p}(r,\theta)$ where the particular solution $T_{i,p}$ is a linear function of r and the homogeneous part is given by Eq. (9), which is a sum of terms proportional to r^{λ_i} with eigenvalues λ_i found from Eq. (8). The smallest λ_i is dominant near the triple-phase line (i.e. near $r = 0$) and if less than one (i.e. $\lambda_1 < 1$), the temperature gradient $\frac{\partial T}{\partial r}$ and thus the heat flux becomes infinite at the triple-phase line. For $\lambda_1 > 1$ the heat fluxes remain finite and the temperature gradients are determined by the particular solution at the triple-phase line. As shown in Eq. (8), the eigenvalues are a function of the thermal conductivities, and the solid and growth angles or $\lambda_i = f(\frac{k_s}{k_l}, \frac{k_g}{k_l}, \theta_s, \theta_{gr})$. In the following, the variations of the eigenvalues of the three-phase analysis with these four parameters, obtained from Eq. (8), are determined and compared to the eigenvalues obtained from two-phase analysis determined from Eq. (10). Any significant difference between two-phase and three-phase analyses indicates that including the inert phase in models of triple-phase lines is important.

The variation of $\lambda_i - 1$ with θ_{gr} is shown in Fig. 3. Negative values of $\lambda_i - 1$ correspond to a singular behavior of $\frac{\partial T}{\partial r}$ at the triple-phase line. This is for a typical HRG-type configuration of silicon where $\theta_s = 55°$, and $k_s/k_l = 0.34$ (same as for numerical simulations in Table 2). In this figure and in the following a subscript of $2ph$ or $3ph$ indicates results from the two-phase or three-phase analysis respectively. For the three-phase results, the thermal conductivity of helium specified in Table 2 was used. There are two distinct behaviors shown in the figure. For θ_{gr} less than around 13°, $\lambda_{1,3ph}$ is not matched by any value of λ from the two-phase analysis, and $\lambda_{1,2ph}$ matches $\lambda_{2,3ph}$. For θ_{gr} greater than 13°, $\lambda_{1,3ph}$ matches $\lambda_{1,2ph}$ and $\lambda_{2,3ph}$ is not matched by any mode in the two-phase analysis. The appearance of additional modes when adding phases was observed by Anderson and Davis [12] and Proudman and Assadullah [10] when comparing the eigenvalues of heat fluxes and flow stresses from a single-phase fluid flow near a wedge with a two-phase flow using a similar singular point analysis.

To explain this behavior, first recall that, as discussed in Section 2.1.2, the particular solutions, which are linear, are different between the two-phase and three-phase analyses. Now, consider the case of $\theta_{gr} = 0$ in Fig. 3, where $\lambda_{1,3ph} = 0.995$. This mode works in conjunction with the three-phase particular solution to reproduce the two-phase behavior. In the absence of radiation, the particular solution of the three-phase model in the solid and melt is simply

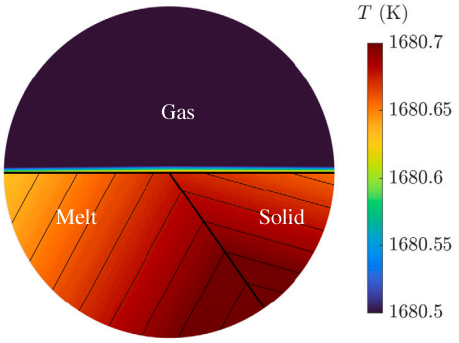

Fig. 4. Temperature contours calculated using the leading terms of the analytic solution for an HRG-type configuration (Table 2). Solution coefficients were chosen to have an average surface heat flux of 150 W/cm^2 over a radius of 1 μm. The range of contour levels was chosen to show temperature variations in the silicon. Gas phase temperature variations quickly exceed the contour range.

$\frac{\rho_s L_f u_{s,1}}{k_l - k_s} x$ (see Eq. (11)) and does not include any heat fluxes from the top surfaces. The vertical heat flux is represented by the first mode of the homogeneous part. For the two-phase analysis, as $\lambda_{1,2ph} > 1$, the linear particular solution (Eq. (12)) is dominant as $r \to 0$.

To show this, we compare temperature contours from the sum of the particular solution and the first term of the homogeneous part of the three-phase model with the linear particular solution of the two-phase model for a radius of 1 μm about the triple-phase line. To determine the unknown coefficient C_1 in Eq. (9), the average convective heat flux through the top surface was set equal to the convective heat flux imposed as a boundary condition for the two-phase model for a radius of 1 μm around the triple-phase line. The heat flux was assumed to be 150 W/cm^2 to match the numerical simulation of Section 3.1.

Fig. 4 shows the three-phase temperature contours for $u_{s,1} = 0.7$ mm/s to match the validation case presented in Section 3.1 where there were no radiation fluxes. Since k_g is much smaller than k_s and k_l, there is a sharp change of temperature in the gas phase, and only a few gas contours are shown so that the liquid and solid phase temperature variations can be seen. The two-phase (not shown) and three-phase contour plots were visually indistinguishable, which confirms that for these conditions, the two-phase and three-phase results are consistent. For non-zero growth angles the value of $\lambda_{1,3ph}$ is not close to one. Thus, the two-phase and three-phase solutions will be different. This is because when there is a non-zero growth angle, it is incorrect in the two-phase analysis to assume that the heat fluxes can be approximated as a constant approaching the triple-phase line. The geometry of the triple-phase line induces rapid variations in gas phase heat transfer in its vicinity.

To verify whether the models are consistent as material properties change, Fig. 5, shows the variation of $\lambda_i - 1$ as a function of k_s/k_l. This is for the same configuration as above but we set $\theta_{gr} = 0$ to eliminate geometrically-induced singularities in the gas as we varied k_s/k_l keeping k_g/k_l and other parameters fixed. The value of k_s/k_l for Si is shown as a vertical line. Here, a similar behavior to Fig. 3 is seen, where there are additional homogeneous modes in the three-phase solution, which represent the gas phase behavior.

For $k_s/k_l > 1$, the first eigenvalue from the three-phase analysis, $\lambda_{1,3ph}$, coincides with the first eigenvalue from the two-phase analysis, $\lambda_{1,2ph}$, indicating that the two-phase and three-phase solutions match for these conditions. Whereas for $k_s/k_l < 1$, $\lambda_{1,2ph}$ parallels $\lambda_{2,3ph}$ and $\lambda_{1,3ph}$ dominates the behavior. Note that the particular solution of the two-phase model should approximately make up for additional eigenvalues of the three-phase solution near 1 (i.e. $\lambda_i - 1 \approx 0$). However, for $k_s/k_l < 1$, even with a flat-top surface geometry, the three-phase solution does not reproduce the linear behavior of the two-phase particular solution and the solution actually becomes singular.

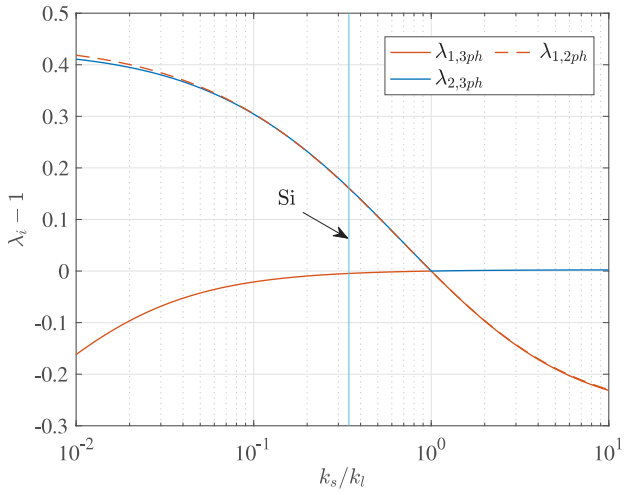

Fig. 5. The variation of the leading order eigenvalues of the analytical homogeneous solution with the ratio of the thermal conductivities k_s/k_l for $\theta_s = 55°$, $\theta_{gr} = 0°$, and $k_g/k_l = 0.0055$.

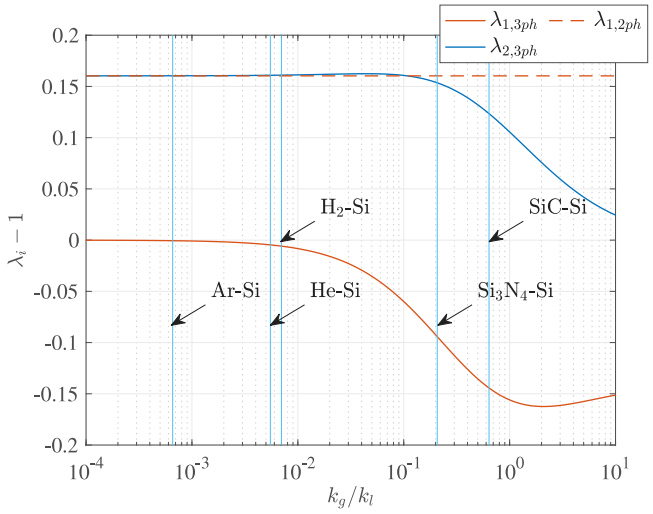

Fig. 6. The variation of the leading order eigenvalues of the analytical homogeneous solution with the ratio of the thermal conductivities k_g/k_l near the triple-phase line of solid facet in contact with its melt with $\theta_s = 55°$, $\theta_{gr} = 0$, and $k_s/k_l = 0.34$. Values of k_g/k_l for three gases and two solids (for confined solidification systems) in contact with solidifying silicon are shown by vertical lines for comparison.

Thus, to accurately model the behavior near the triple-phase line all three phases must be included for these conditions.

The variation of $\lambda_i - 1$ with k_g/k_l is shown in Fig. 6 for the same configuration. Here the value of k_s/k_l for silicon (0.34) was used, but the behavior for gallium arsenide with $k_s/k_l = 0.5$ [30] is similar. The plot also indicates approximate values of k_g/k_l for argon [21], helium [19], hydrogen [19], and also silicon nitride [31] and silicon carbide [31] for confined growth in a crucible. The eigenvalues become sensitive to k_g/k_l for $k_g/k_l > 0.01$. For these values of k_g/k_l the singular behavior of the solution at the triple-phase line can only be seen from a three-phase analysis. Such larger values of k_g/k_l are possible for confined growth of silicon within a crucible and even higher values of k_g/k_l are obtained for melts with lower thermal conductivities such as GaAs where $k_s = 7$ W/(m K) and $k_l = 14$ W/(m K) [30].

Fig. 7 illustrates the leading order eigenvalues of the homogeneous solution as a function of θ_s again for an HRG-type configuration ($k_s/k_l = 0.34$, and $k_g/k_l = 0.0055$, and $\theta_{gr} = 11°$). The solid angles corresponding to (111) and ($\bar{1}$11) facets assuming [$\bar{1}$11] is upward are

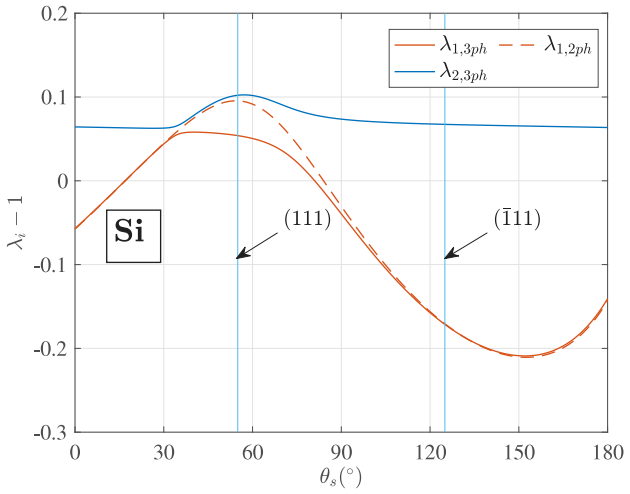

Fig. 7. The variation of the leading order eigenvalues of the analytical homogeneous solution with the solid angle θ_s for silicon ($\theta_{gr} = 11°$, $k_s/k_l = 0.34$, and $k_g/k_l = 0.0055$).

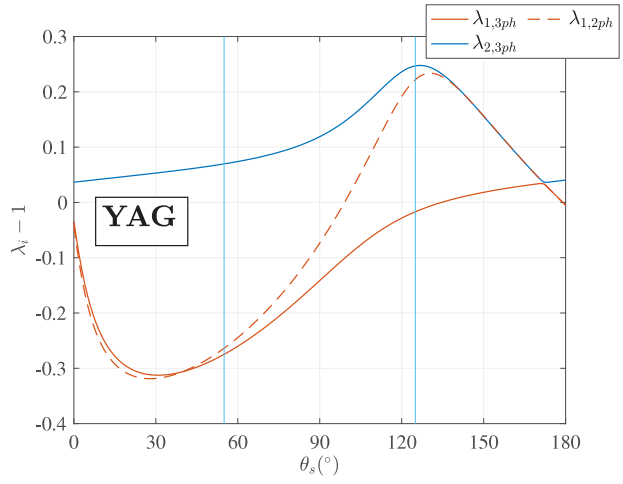

Fig. 8. The variation of the leading order eigenvalues of the analytical homogeneous solution with the solid angle θ_s for Yttrium Aluminum Garnet (YAG) ($\theta_{gr} = 8°$, $k_s/k_l = 8.4$, and $k_g/k_l = 0.11$).

also identified with a vertical line. Both (1̄11) and (111) facets were observed experimentally by Kellerman et al. [2] and analyzed by Pirnia and Helenbrook [3]. Note that the temperature gradient approaches infinity for the (1̄11) facet at the triple-phase line whereas it is bounded for a (111) facet, consistent with the two-phase predictions.

In Fig. 8 the changes of $\lambda_i - 1$ with θ_s are shown for YAG in contact with its melt and helium with $\theta_{gr} = 8°$ [32], $k_s/k_l = 8.4$, and $k_g/k_l = 0.11$. The thermal conductivities at the melting point of YAG, 2243 K, were used with k_l and k_s from [15] and k_g from the correlation for monatomic gases in [21]. YAG tends to do the opposite of Si because in contrast to silicon, for YAG $k_s > k_l$. For example, the temperature gradient at the triple-phase line for $\theta_s = 55°$ is singular whereas at $\theta_s = 135°$ it is finite. Also note that, for $100° < \theta_s < 135°$ the three-phase analysis indicates infinite temperature gradients whereas the two-phase analysis indicates the temperature gradients to be finite at the triple-phase line.

3.1. Validation

To validate the above predictions, a three-phase simulation of horizontal ribbon growth of silicon forming a (111) facet with $\theta_s = 55°$ and

Table 4
Validation of the second eigenvalue for solid silicon in contact with its melt and helium with $\theta_s = 55°$, and $\theta_{gr} = 0$ using the exponent of the curve fit $\frac{\partial T}{\partial r} = ar^b + c$ along the solid-gas (SG), solid-melt (SL), and melt-gas (LG) interfaces on three nested grids.

Grid/ Extrapolation	DOF	b_{SG}	b_{SL}	b_{LG}
Coarse	113×10^3	0.112	0.0707	0.398
Medium	445×10^3	0.166	0.143	0.252
Fine	176×10^4	0.181	0.161	0.203
Extrapolation	–	0.187	0.168	0.179
Analytical	–	0.161	0.161	0.161

cooled by a helium jet was performed. The contour plot for temperature is shown in Fig. 9 for the case with $\theta_{gr} = 0$ and no radiation. The greatest temperature changes are in the gas phase where the cold jet exiting the slot at $T = 300$ K heats up to about T_m. A zoomed-in view of the region close to the triple-phase line is shown in Fig. 9 as well. The radius of the zoomed-in view circle is 1 μm, which is the same radial distance used for Fig. 4 of analytical solution with matching heat flux. The agreement between the zoomed-in view and Fig. 4 qualitatively affirms the validity of the analysis. Recall that the average heat flux at the top melt and solid surfaces over $r < 1$ μm from this numerical simulation (150 W/cm^2) was used to determine the unknown coefficient C_1 for the leading-order term in the homogeneous part of the analytical solution of temperature (Eq. (9)).

Fig. 10 shows temperature along the interfaces for Figs. 9 and 4. Note that as $r \to 0$ the radial temperature gradients from the numerical simulation approach the values of the analytical solution. This shows that as $r \to 0$ the leading-order terms become dominant. At larger values of r the differences increase as the higher modes are not negligible. The analytical solution is the linear particular solution and the first term of the homogeneous solution corresponding to $\lambda_{1,3ph} = 0.995$ and the second term with $\lambda_{2,3ph} = 1.161$ was neglected. For cases like these where not only the particular part of the solution is linear but also the first two eigenvalues are close to linear, distinguishing the dominant leading-order terms was difficult. Note that when leading order eigenvalues deviate significantly from 1 (e.g. as shown by $k_s/k_l = 0.01$ in Fig. 5 or $\theta_s = 30°$ in Fig. 8), the magnitude of the higher modes should become negligible at larger values of r than Fig. 10.

To validate the eigenvalues of the homogeneous part of the solution, curves of the form $ar^b + c$, with the parameters a, b, and c, were fit to $\frac{\partial T}{\partial r}$ of the numerical solution along various surfaces for $r < 1$ μm to identify the exponent b. Fig. 11 shows the data and curve fits for the case with $\theta_{gr} = 0$ and no radiation and Table 4 gives the curve fit values. This is a non-singular case so the $\frac{\partial T}{\partial r}$ values are expected to remain finite. Because the first mode was so close to linear, the constant of the curve fit actually incorporates the particular solution and the first mode, and the curve fit exponent matched $\lambda_{2,3ph} = 1.161$. A Richardson extrapolation was performed on a set of nested grids with the extrapolated values listed on the last row of Table 4, and values close to the analytical value of $\lambda_2 - 1 = 0.161$ were obtained.

To validate the particular part of the solution, for the case with $\theta_{gr} = 11°$ and radiation, using $\lambda_1 = 1.054$ and $\lambda_2 = 1.102$ from the analytical solution, curves of the form $ar^{\lambda_1 - 1} + br^{\lambda_2 - 1} + c$ were fit to $\frac{\partial T}{\partial r}$ values. The constant c of the curve fit should be close to the value from the gradient of the particular solution. The results using a set of nested grids are shown in Table 5, which agrees reasonably with analytical values although accurate values were difficult to obtain. The mesh was refined to a level of about 10 nm. Even with this resolution, the solution had numerical oscillations near the triple-phase line, which affected the quality of the curve fit. In any case, these results confirm that there is both qualitative and quantitative agreement between the full numerical solutions and the analysis.

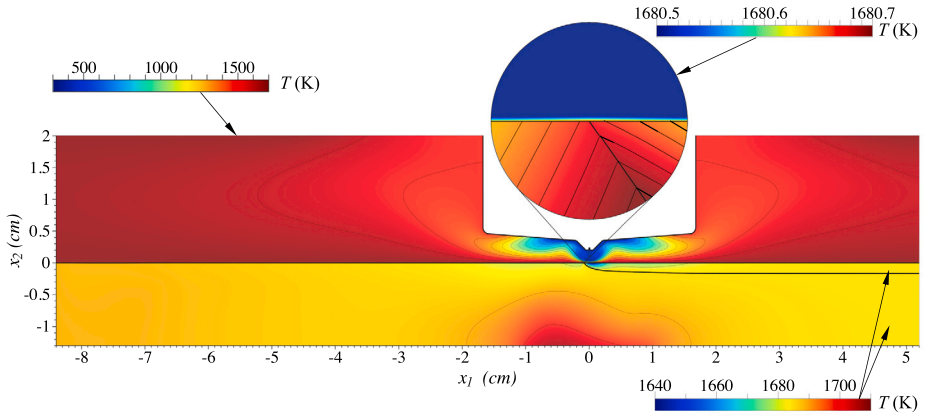

Fig. 9. The temperature contour plot for horizontal ribbon growth of silicon at a pull speed of $u_{s,1} = 0.7$ mm/s cooled by a helium jet for $\theta_{gr} = 0$. The contour lines are 100 K apart in the gas. The contour lines in the zoomed-in view are 0.01 K apart. For the solid and melt the temperature contours are 10 K apart.

Table 5
Validation of the particular part of the analytical solution for solid silicon in contact with its melt and helium with $\theta_s = 55°$ and $\theta_{gr} = 11°$ using the constant c of the curve fit $\frac{\partial T}{\partial r} = ar^{\lambda_1 - 1} + br^{\lambda_2 - 1} + c$ along the solid-gas (SG), solid-melt (SL), and melt-gas (LG) interfaces on three nested grids with the values of $\lambda_1 = 1.054$ and $\lambda_2 = 1.102$ from the analytical homogeneous solution.

Grid/Extrapolation/Analytical	DOF	c_{SG} (K/mm)	c_{SL} (K/mm)	c_{LG} (K/mm)
Coarse	130×10^3	144.5	89.4	−99.6
Medium	510×10^3	130.5	81.5	−109.8
Fine	202×10^4	133.5	80.8	−106.3
Extrapolation	–	–	80.7	–
Analytical	–	146.0	83.9	−117.2

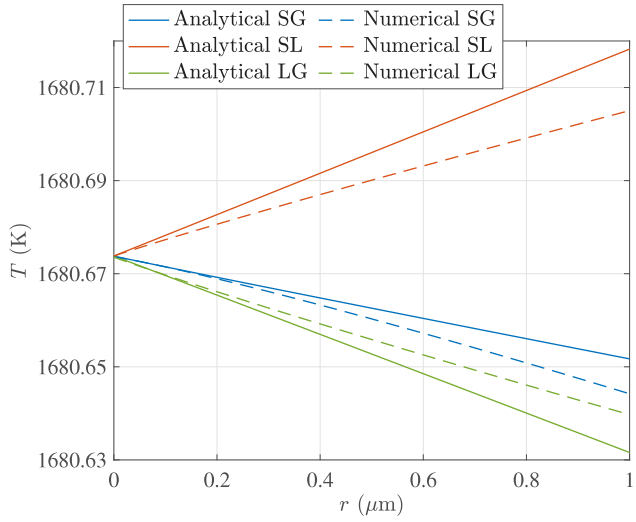

Fig. 10. Temperature along the solid-gas (SG), solid-melt (SL), and liquid-gas (LG) interfaces for the zoomed-in view of the numerical simulation shown in Fig. 9 and the leading order terms of the analytical solution shown in Fig. 4.

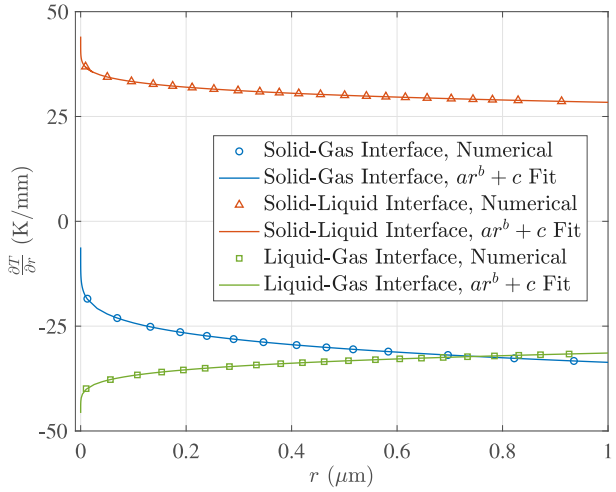

Fig. 11. The curve fits $ar^b + c$ to the numerical solution of $\frac{\partial T}{\partial r}$ for the triple-phase line of solid silicon in contact with its melt and helium with $\theta_s = 55°$ and $\theta_{gr} = 0$ along the solid-gas, solid-melt, and melt-gas interfaces using the fine mesh of Table 4. Only one in every four values of $\frac{\partial T}{\partial r}$ is shown for clarity.

4. Conclusions

The local behavior of the analytical solution of the temperature field near the triple-phase line of a solid crystal in contact with its melt and an inert phase was determined and validated. It was shown that the eigenvalues were a function of the ratio of the thermal conductivities of the three materials meeting at the triple-phase line, the solid angle, and the growth angle. The two-phase analysis, which neglects the effect of the inert phase and the three-phase analysis generally agree but the three-phase solution includes additional modes to describe the gas behavior. The difference in the particular solutions of the two-phase and three-phase models can approximately make up for the leading order eigenvalue missing from the three-phase analysis.

There are some ranges of conditions where the two-phase and three-phase analyses predict different behaviors (singular versus non-singular temperature gradients for example). Also, especially with a growth angle, it is not correct to assume gas phase heat flux is constant near the triple-phase line in the two-phase analysis. For triple-phase lines where the thermal conductivity of the inert phase is much smaller than that of the melt and solid, the two-phase model did not significantly change the leading-order eigenvalues. However, the two-phase and three-phase analysis can give different behaviors for triple-phase lines

when the thermal conductivity of the inert phase is comparable to the solid or melt (e.g. in confined solidification systems). Therefore, for numerical simulations involving triple-phase lines, especially if the thermal conductivity of the inert phase is comparable to solid or melt, the local temperature behavior near the triple-phase line from three-phase and two-phase assumptions should be compared using Eqs. (8) and (10) respectively before neglecting the inert phase and using a simpler two-phase simulation.

CRediT authorship contribution statement

Nojan Bagheri-Sadeghi: Methodology, Software, Validation, Formal analysis, Investigation, Writing – original draft, Visualization. **Brian T. Helenbrook:** Conceptualization, Methodology, Software, Resources, Writing – review & editing, Supervision, Project administration, Funding acquisition.

Declaration of competing interest

The authors declare that they have no known competing financial interests or personal relationships that could have appeared to influence the work reported in this paper.

Data availability

Data will be made available on request.

Acknowledgments

This material is based upon work supported by the National Science Foundation, United States under Grant No. 1762802. Some of the computing for this project was performed on the ACRES cluster. We would like to thank Clarkson University and the Office of Information Technology for providing computational resources and support that contributed to these research results. Additional computational resources for this grant were provided by the National Science Foundation, United States under Grant No. 1925596.

References

[1] V.S. Ajaev, S.H. Davis, The effect of tri-junction conditions in droplet solidification, J. Cryst. Growth 264 (1) (2004) 452–462, http://dx.doi.org/10.1016/j.jcrysgro.2003.11.119.

[2] P. Kellerman, B. Kernan, B.T. Helenbrook, D. Sun, F. Sinclair, F. Carlson, Floating silicon method single crystal ribbon – observations and proposed limit cycle theory, J. Cryst. Growth 451 (2016) 174–180, http://dx.doi.org/10.1016/j.jcrysgro.2016.07.012.

[3] A. Pirnia, B.T. Helenbrook, Physics of double faceted crystal growth in solidification processes, J. Cryst. Growth 582 (2022) 126517, http://dx.doi.org/10.1016/j.jcrysgro.2022.126517.

[4] N. Eustathopoulos, B. Drevet, S. Brandon, A. Virozub, Basic principles of capillarity in relation to crystal growth, in: T. Duffar (Ed.), Crystal Growth Processes Based on Capillarity, John Wiley & Sons, 2010, pp. 1–49, http://dx.doi.org/10.1002/9781444320237.ch1, Ch. 1.

[5] N. Bagheri-Sadeghi, B.T. Helenbrook, Buoyancy and Marangoni effects on horizontal ribbon growth, J. Cryst. Growth 596 (2022) 126822, http://dx.doi.org/10.1016/j.jcrysgro.2022.126822.

[6] R.A. Brown, Theory of transport processes in single crystal growth from the melt, AIChE J. 34 (6) (1988) 881–911, http://dx.doi.org/10.1002/aic.690340602.

[7] D.M. Anderson, S.H. Davis, Local fluid and heat flow near contact lines, J. Fluid Mech. 268 (1994) 231–265, http://dx.doi.org/10.1017/S0022112094001333.

[8] W.R. Dean, P.E. Montagnon, On the steady motion of viscous liquid in a corner, Math. Proc. Camb. Phil. Soc. 45 (3) (1949) 389–394, http://dx.doi.org/10.1017/S0305004100025019.

[9] H.K. Moffatt, Viscous and resistive eddies near a sharp corner, J. Fluid Mech. 18 (1) (1964) 1–18, http://dx.doi.org/10.1017/S0022112064000015.

[10] I. Proudman, M. Asadullah, Steady viscous flow near a stationary contact line, J. Fluid Mech. 187 (1988) 35–43, http://dx.doi.org/10.1017/S0022112088000321.

[11] D.M. Anderson, S.H. Davis, Two-fluid viscous flow in a corner, J. Fluid Mech. 257 (1993) 1–31, http://dx.doi.org/10.1017/S0022112093002976.

[12] D. Anderson, S. Davis, Fluid flow, heat transfer, and solidification near tri-junctions, J. Cryst. Growth 142 (1) (1994) 245–252, http://dx.doi.org/10.1016/0022-0248(94)90293-3.

[13] B.T. Helenbrook, Solidification along a wall or free surface with heat removal, J. Cryst. Growth 418 (2015) 79–85, http://dx.doi.org/10.1016/j.jcrysgro.2015.02.028.

[14] A. Pirnia, B.T. Helenbrook, Analysis of faceted solidification in the horizontal ribbon growth crystallization process, J. Cryst. Growth 555 (2021) 125958, http://dx.doi.org/10.1016/j.jcrysgro.2020.125958.

[15] O. Weinstein, S. Brandon, Dynamics of partially faceted melt/crystal interfaces i: Computational approach and single step–source calculations, J. Cryst. Growth 268 (1) (2004) 299–319, http://dx.doi.org/10.1016/j.jcrysgro.2004.04.108.

[16] V.V. Voronkov, Supercooling at the face developing on a rounded crystallization front, Sov. Phys. – Crystallogr. 17 (5) (1973) 807–813.

[17] D. Buta, M. Asta, J.J. Hoyt, Kinetic coefficient of steps at the Si(111) crystal-melt interface from molecular dynamics simulations, J. Chem. Phys. 127 (7) (2007) 074703, http://dx.doi.org/10.1063/1.2754682.

[18] B.T. Helenbrook, P. Kellerman, F. Carlson, N. Desai, D. Sun, Experimental and numerical investigation of the horizontal ribbon growth process, J. Cryst. Growth 453 (2016) 163–172, http://dx.doi.org/10.1016/j.jcrysgro.2016.08.034.

[19] T. Bergman, T. Bergman, F. Incropera, D. DeWitt, A. Lavine, Fundamentals of Heat and Mass Transfer, Seventh Ed., Wiley, 2011.

[20] M. Mito, T. Tsukada, M. Hozawa, C. Yokoyama, Y.-R. Li, N. Imaishi, Sensitivity analyses of the thermophysical properties of silicon melt and crystal, Meas. Sci. Technol. 16 (2) (2005) 457–466, http://dx.doi.org/10.1088/0957-0233/16/2/018.

[21] R. Bird, W. Stewart, E. Lightfoot, Transport Phenomena, second ed., Wiley, 2002.

[22] F. White, Fluid Mechanics, Seventh Ed., McGraw-Hill, 2011.

[23] B. Helenbrook, J. Hrdina, High-order adaptive arbitrary-Lagrangian–Eulerian (ale) simulations of solidification, Comput. & Fluids 167 (2018) 40–50, http://dx.doi.org/10.1016/j.compfluid.2018.02.028.

[24] N. Bagheri-Sadeghi, V.A. Fabiyi, B.T. Helenbrook, E. Paek, Sensitivity of horizontal ribbon growth to solidification kinetics, J. Cryst. Growth 603 (2023) 127038, http://dx.doi.org/10.1016/j.jcrysgro.2022.127038.

[25] J.R. Howell, M.P. Mengüç, R. Siegel, Thermal Radiation Heat Transfer, Sixth Edition, CRC Press, 2016, http://www.thermalradiation.net/sectionb/B-71.html.

[26] B. Helenbrook, A two-fluid spectral-element method, Comput. Methods Appl. Mech. Engrg. 191 (3) (2001) 273–294, http://dx.doi.org/10.1016/S0045-7825(01)00275-4.

[27] N. Zuckerman, N. Lior, Jet impingement heat transfer: Physics, correlations, and numerical modeling, in: Vol. 39 of Advances in Heat Transfer, Elsevier, 2006, pp. 565–631, http://dx.doi.org/10.1016/S0065-2717(06)39006-5.

[28] S. Sherwin, G. Karniadakis, A triangular spectral element method; applications to the incompressible Navier–Stokes equations, Comput. Methods Appl. Mech. Engrg. 123 (1) (1995) 189–229, http://dx.doi.org/10.1016/0045-7825(94)00745-9.

[29] S. Balay, S. Abhyankar, M.F. Adams, S. Benson, J. Brown, P. Brune, K. Buschelman, E. Constantinescu, L. Dalcin, A. Dener, V. Eijkhout, J. Faibussowitsch, W.D. Gropp, V. Hapla, T. Isaac, P. Jolivet, D. Karpeev, D. Kaushik, M.G. Knepley, F. Kong, S. Kruger, D.A. May, L.C. McInnes, R.T. Mills, L. Mitchell, T. Munson, J.E. Roman, K. Rupp, P. Sanan, J. Sarich, B.F. Smith, S. Zampini, H. Zhang, H. Zhang, J. Zhang, PETSc/TAO Users Manual, Tech. Rep. ANL-21/39 - Revision 3.19, Argonne National Laboratory, 2023, http://dx.doi.org/10.2172/1968587.

[30] J. Derby, R. Brown, Thermal-capillary analysis of Czochralski and liquid encapsulated czochralski crystal growth: I. simulation, J. Cryst. Growth 74 (3) (1986) 605–624, http://dx.doi.org/10.1016/0022-0248(86)90208-3.

[31] G.W.C. Kaye, T.H. Laby, Tables of Physical and Chemical Constants, sixteenth Ed., Longman Scientific & Technical, 1995.

[32] R. Feigelson, Pulling optical fibers, J. Cryst. Growth 79 (1, Part 2) (1986) 669–680, http://dx.doi.org/10.1016/0022-0248(86)90535-X, proceedings of the Eighth International Conference on Crystal Growth.